https://doi.org/10.5194/egusphere-2026-2519
Preprint. Discussion started: 11 June 2026

High Spatial and temporal 3D Sea Ice Thickness Reconstruction Using Seismic Waveform Inversion and Tomography

Hooshmand Zandi[1], Ludovic Métivier[1], Romain Brossier[1], Sebastien Kuchly[2], Vasco Zanchi[2], Nicolas Mokus[2], Véronique Dansereau[1], Antonin Eddi[2], Stéphane Perrard[3], Dany Dumont[3], and Ludovic Moreau[1]

[1]Institut des Sciences de la Terre, Université Grenoble Alpes, Grenoble, France
[2]PMMH-ESPCI, Paris, France
[3]Institut des sciences de la mer, Université du Québec à Rimouski, Québec G5L 3A1 Canada

Correspondence: Ludovic Moreau (ludovic.moreau@univ-grenoble-alpes.fr)

Abstract. Sea ice is a porous, two-phase material whose evolution influences climate, ecosystems, and human activities in polar regions. Rapid declines in Arctic sea ice thickness highlight the need for monitoring approaches that resolve small-scale spatial variability, beyond the coarse resolution of satellite-derived products. Seismic methods, based on the analysis of seismic waves guided in the ice layer, provide high-resolution local estimates of ice thickness, but have so far been limited to individual source–receiver paths. Here, we present a methodology to generate maps of sea ice thickness from seismic data. We analyze two complementary datasets acquired on fast ice: controlled-source data recorded by a 16-geophone array in the St. Lawrence Estuary (Canada), and passive data collected by a dense 247-geophone array in Svalbard (Norway). Ice thickness is first estimated along individual paths through waveform inversion based on spectral element modeling. These path-specific estimates are then integrated within a tomographic framework to reconstruct spatially continuous sea ice thickness maps. Our results demonstrate that both active and passive seismic measurements can resolve spatial heterogeneity in ice thickness at high resolution. This seismic-tomographic approach provides a practical and scalable tool for fine-scale monitoring of sea ice in rapidly changing polar environments.

1 Introduction

Over the past decades, Arctic sea ice has declined dramatically in both extent and thickness, primarily due to climate warming, with the greatest losses occurring in late summer and early autumn. Between 2010 and 2019, the average Arctic sea ice area from August to October was about 25% smaller than in 1979–1988, while ice volume fell by roughly 72% between 1979 and 2016 (Kim et al., 2023). Recent studies project a seasonally ice-free Arctic around 2040, earlier than many climate models had predicted (Schweiger et al., 2019; Comiso et al., 2017; Stroeve and Notz, 2018; Kim et al., 2023). Its rapid decline increases sunlight penetration and open-water areas, altering ocean conditions, enhancing vertical mixing, and enabling not only the traditional spring phytoplankton bloom but also a new fall bloom in some regions (Ardyna et al., 2014). These ecological shifts signal a transition from a single short growing season to a more temperate-like regime with two productive periods, affecting marine food webs and key species. At the same time, ice loss drives societal impacts: Indigenous and local communities face

https://doi.org/10.5194/egusphere-2026-2519
Preprint. Discussion started: 11 June 2026

changes in wildlife, livelihoods, culture, and infrastructure, while reduced ice cover opens new opportunities for shipping and resource development, creating adaptation challenges (Post et al., 2013; Ford et al., 2021).

Despite advances in observations and modeling, significant uncertainties remain, highlighting the urgent need for improved forecasting and adaptation strategies. While previous models have relied primarily on large-scale sea ice parameters, understanding the rapid changes in sea ice dynamics under geophysical forcing requires monitoring sea ice properties at finer spatial and temporal scales. Field data are crucial for understanding sea ice dynamics and properties and are obtained through remote and indirect measurement techniques. Accurate methods such as ice-profiling sonar enable estimates of ice thickness, drift, and topography (Fissel et al., 2008), but they are limited by high cost and restricted spatial and temporal coverage. Ground-penetrating radar (GPR) similarly provides ice and snow thickness estimates (Matsumoto et al., 2019), yet remains constrained to short-term field campaigns due to logistical challenges. Because polar regions are harsh and largely inaccessible, in situ observations are sparse, making satellite remote sensing the primary tool for large-scale sea ice monitoring.

Sea ice thickness (SIT)—a key climate variable affecting heat exchange, mass balance, and freshwater fluxes—is usually derived from radar and laser altimetry, which provide extensive spatial coverage and long-term records (Mäkynen et al., 2020). Traditional monthly averaged SIT maps, however, neglect ice motion and short-term dynamics, causing spatial blurring and regional biases. Drift-aware approaches (DA-SIT) improve accuracy by accounting for motion and dynamic changes (Ricker et al., 2025).

Seismic methods offer an alternative for estimating ice thickness at small scales and over local areas. By recording and analyzing seismic waves guided in the ice, they can infer ice properties and thickness with high resolution and enable continuous monitoring. This makes them a valuable complement to satellite and large-scale in situ observations, which are often limited in space or time. Initial work by Ewing et al. (1934); Ewing and Crary (1934) established relationships between wave velocity and ice elasticity, identifying longitudinal, horizontally polarized shear (SH), and dispersive flexural waves. Subsequent studies of air-coupled flexural waves (ACFWs) showed how coupling with air and water modifies dispersion, enabling estimation of elastic constants and thickness from measured wave velocities in Arctic field campaigns (Press and Ewing, 1951; Press, 1951a; Oliver et al., 1954; Hunkins, 1960).

Numerical modeling and inversion methods developed from the 1980s onward allowed determination of ice thickness and elastic properties from flexural and longitudinal waves recorded on first- and multi-year pack ice (Miller and Schmidt, 1991; Wang, 1995; Yang and Giellis, 1994; Yang and Yates, 1995; Stein et al., 1998). Air-coupled flexural waves (ACFWs) provide a practical method for monitoring ice thickness. Romeyn et al. (2021) developed a theoretical framework for reliably estimating ice thickness, and Romeyn and Hanssen (2023) showed that simple microphones with natural or artificial sources can provide accurate measurements. Other studies examined the spatial variability and heterogeneity of ice. Rajan et al. (1993) used crosshole tomography to measure P- and S-wave velocities in multi-year ice, revealing low-velocity zones likely due to high brine content and enabling estimates of Poisson's ratio, salinity, elastic moduli, and attenuation. Xie and Farmer (1994) showed that ice ridges and impact angles affect damping, wave velocities, and acoustic radiation, emphasizing energy loss through ice damage. Xu et al. (2025) applied high-resolution tomography to summer Arctic ice, revealing vertically layered structures with

https://doi.org/10.5194/egusphere-2026-2519
Preprint. Discussion started: 11 June 2026

near-surface attenuation caused by partial melting and temperature effects, thereby improving understanding of acoustic wave behavior.

In parallel, theoretical and modeling studies have provided insights into ice behavior under dynamic loads. Squire et al. (1996) modeled moving loads on floating ice as thin elastic or viscoelastic plates, identifying a critical speed at which wave energy accumulates, causing large deflections. Landschulze (2018) used finite-element simulations to capture flexural, longitudinal, and higher-mode waves, showing that numerical approaches more accurately represent high-frequency effects, wave interactions, and mode conversions than analytical plate-theory models. Johansen et al. (2019) applied full-waveform modeling to optimize source–receiver configurations for Arctic surveys, demonstrating the advantages of numerical methods and providing practical guidance for seismic acquisition while improving understanding of wave propagation in sea ice.

All the aforementioned studies rely on controlled sources. A less labor-intensive and more cost-effective alternative is to use passive approaches where ambient noise, or the signal generated by natural sources is recorded. Marsan et al. (2012, 2019) applied for instance noise interferometry techniques (Shapiro and Campillo, 2004; Sabra et al., 2005), to measure ice thickness from flexural waves and to study flexural and horizontally polarized shear waves.

Building upon the laboratory-scale research conducted by Moreau et al. (2017), Moreau et al. (2020a) applied the method to natural sources data acquired on sea ice to estimate ice thickness and mechanical properties. Using array processing, they derived dispersion curves of seismic guided waves. From the dispersion curves of longitudinal and SH waves, they estimated Young's modulus and Poisson's ratio, given the densities of ice and water. To determine ice thickness, the observed flexural-wave dispersion curves were compared with those obtained from forward modeling using the Finite Element Method (FEM). In a follow-up study, Moreau et al. (2020b) introduced a method that reduced instrumentation requirements by an order of magnitude. Using passive data recorded on only 3–5 receivers, they inferred ice thickness through Bayesian inversion, comparing recorded icequake waveforms with synthetic ones generated using the forward model of Stein (1986). Similarly, Serripierri et al. (2022) used ambient noise correlations to derive dispersion curves of guided waves, which were jointly inverted for elastic constants, density, and thickness of fast ice, demonstrating the potential of passive data for continuous ice monitoring. Moreau et al. (2023) analyzed thousands of icequakes recorded on fast ice in Svalbard. Using a deep convolutional neural network, they clustered thousands of icequake waveforms and successfully isolated the flexural mode. Bayesian inversion of these waveforms was applied to locate icequake sources and estimate the average ice thickness along the source–receiver paths.

In this study, we aim at going beyond this estimation of the ice-thickness along wave paths by proposing 2D maps of the ice thickness, using a tomography-like approach. Each thickness along a given wave path can be interpreted as a travel-time between a source and a receiver and a regionalization strategy similar to what is used for travel-time tomography can be used to generate smooth 2D regionalization of the ice thicknesses. This regionalization is all the more meaningful when dense receiver networks are used. Besides, our approach relies on a multi-stage strategy, where the source localization is performed as a first step, and the thickness along each wave path further determined by a grid search method. Another novelty we introduce is to base these inversion on data computed using a finite element approach and stored in a data base, as an offline computation prior to the inversion. This ensures a more accurate modeling of the very dispersive flexural waves along a wide frequency band, compared with previously used asymptotic approaches. To illustrate the effectiveness of the method, we use

https://doi.org/10.5194/egusphere-2026-2519
Preprint. Discussion started: 11 June 2026

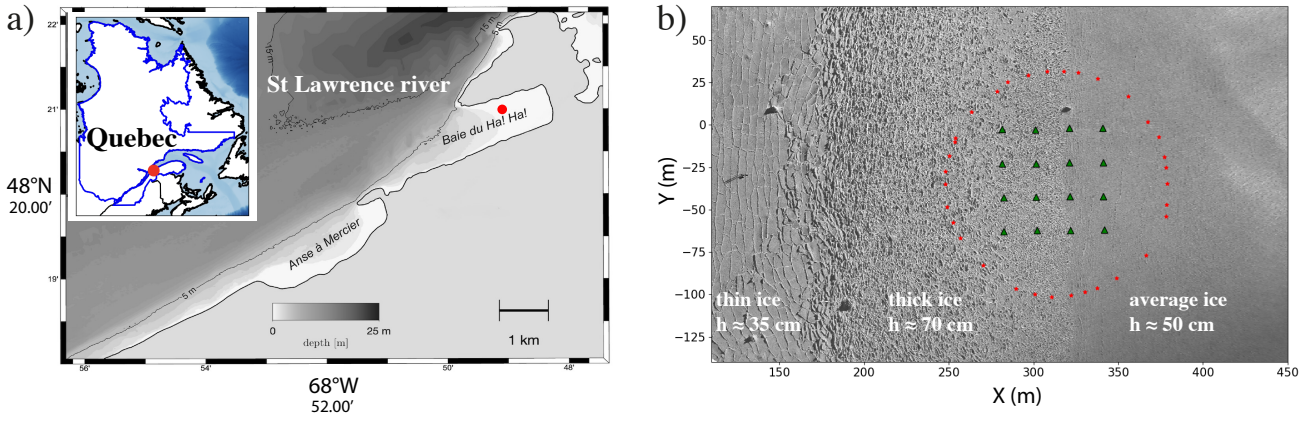

Figure 1. a) Location of Baie du Ha! Ha! in Bic National Park on the St. Lawrence Estuary (Canada). The red dot indicates the site of the experiment. b) Aerial photograph of the fast ice in Baie du Ha! Ha!, showing the positions of the 16 geophones (green triangles) and 33 controlled sources (red stars), placed across two fused ice blocks of different thicknesses.

two complementary datasets: (i) controlled-source data recorded using a small array of 16 geophones deployed on fast ice in the St. Lawrence Estuary (Canada), and (ii) natural-source data collected with a dense array of 247 geophones on fast ice in Svalbard (Norway). On the latter dataset, owing to the deployment period spanning a month, we can produce 2D ice thickness maps at different times, as a first attempt to track the temporal evolution of the ice thickness.

The remainder of this study is organized as follows. In Section 2, we first introduce these two datasets, then we present the different methods related to modeling and inversion to generate 2D ice thickness maps from the data. In Section 3, we present the application of these methods to the two datasets. In Section 4, we discuss the results we obtain and the potential improvements of the methodology which is set up. A conclusion Section ends the study.

2 Materials and Methods

2.1 Data

2.1.1 Controlled-source data

The first dataset consists of seismic data where controlled sources were generated all around an array of geophones placed on fast ice in the St. Lawrence Estuary (Canada). The location of the experiment is the Baie du Ha! Ha! in the Bic National Park (Figure 1a), located on the south shore of the St. Lawrence Estuary. Data were recorded during the 2025 BicWin campaign on 6th February 2025, following the same procedure as the one described in Kuchly et al. (2025) for their dataset in 2024: a square array of 16 three-components (3C) geophones (SmartSolo IGU-16HR, 3C 5 Hz), arranged in 4 lines and 4 columns with 15 m spacing, was deployed on sea ice. Vertical and horizontal sources were generated using hammer shots at 33 positions along a circle with a radius of 60 m, whose center coincided with that of the array (Figure 1b).

https://doi.org/10.5194/egusphere-2026-2519
Preprint. Discussion started: 11 June 2026

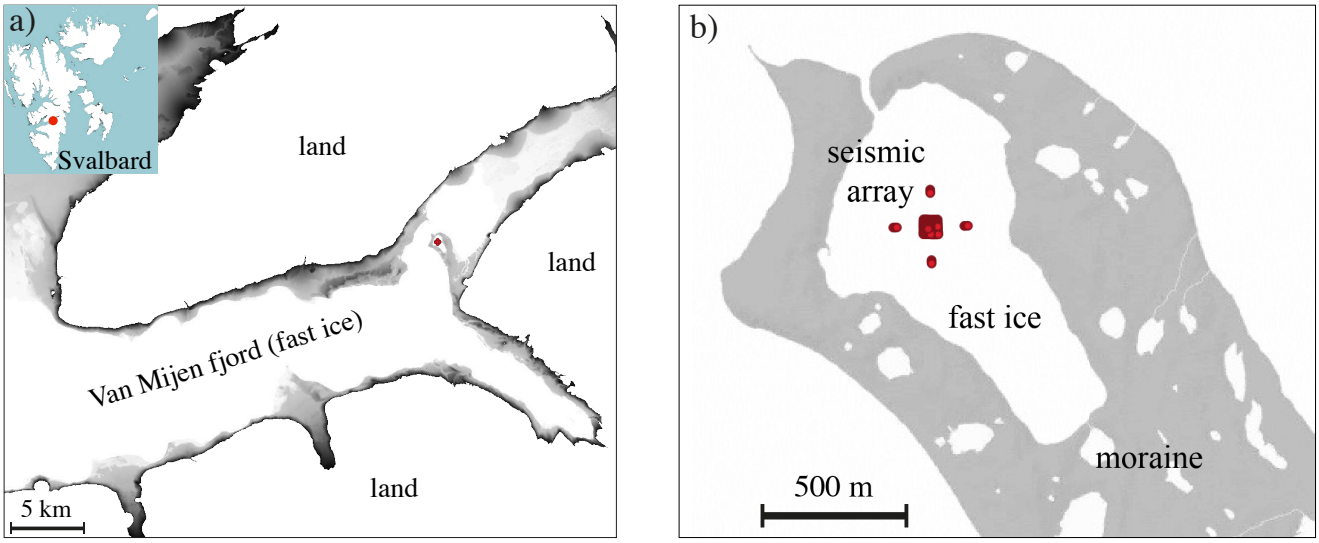

Figure 2. a) The Van Mijen Fjord in Svalbard (Norway), and the array of geophones for the passive experiment.

The ice conditions at and around the array were unusual, with two ice blocks of different thicknesses fused along a line crossing the array (Figure 1b). Drillings in these two blocks indicated average thicknesses of 50 ± 5 cm in the block to the right-hand side of the array, and 70 ± 5 cm in the block to its left-hand side. However, the underside of the ice, below the waterline, was neither solid nor rigid. Instead, it consisted of material intermediate between frazil ice and highly porous ice. Therefore, ice-thickness measurements obtained from drillings may be overestimated by a few centimeters. The thickness of the rigid, consolidated ice was approximately 45 ± 5 cm in the thinner block and 65 ± 5 cm in the thicker one.

2.1.2 Natural-source data

The second dataset consists of natural-source seismic data, in which icequakes act as sources and are recorded by a dense array of geophones deployed on fast ice. Here, we revisit the icequake catalog introduced in Moreau et al. (2023), which was extracted through automatic clustering from the dataset presented in Moreau et al. (2020a). This dataset was acquired in Van Mijen Fjord, Svalbard (Norway) (Moreau and RESIF, 2019), using an array of 247 geophones. The array includes both 1C and 3C FairField Zland geophones (cut-off frequency of 5 Hz), which recorded the ambient seismic field at a sampling frequency of 500 Hz. The main array was arranged in a square with a lateral size of 50 m. Four linear arrays, each consisting of four geophones, were installed 150 m to the north, east, south, and west of the main array, as shown in Figure 2. On average, the inter-station distance was 4 m. The catalog extracted from this dataset contains thousands of icequakes recorded on sea ice between 28 February and 24 March 2019. During the recording period, temperatures were around -25 °C in the first half of March and then rose to around -5 °C in the second half.

https://doi.org/10.5194/egusphere-2026-2519
Preprint. Discussion started: 11 June 2026

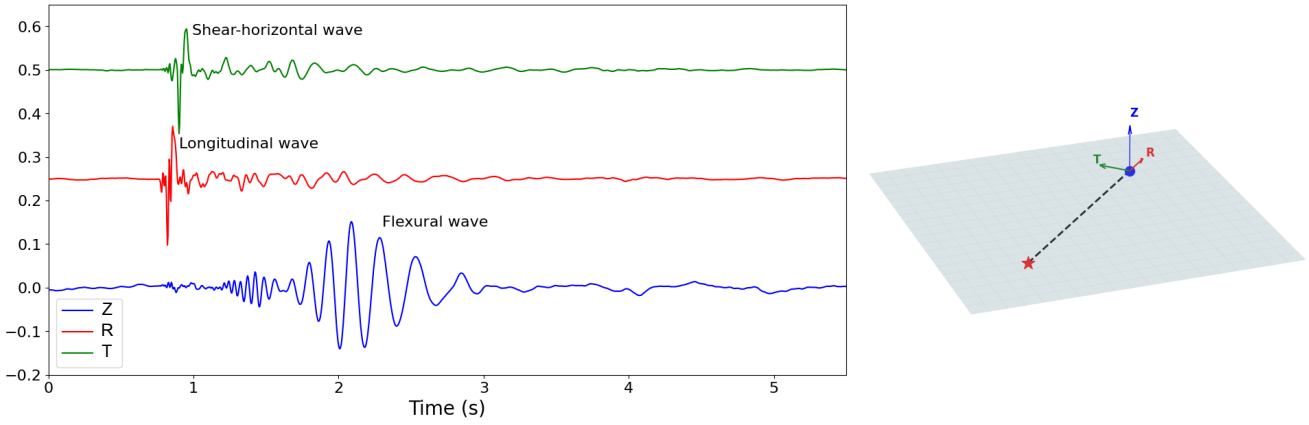

Figure 3. (Left) Example seismic signals recorded on sea ice showing different wave arrivals. (Right) Conceptual illustration of the dominant polarization of the three fundamental guided wave modes in the ice layer.

2.2 Forward Modeling of Seismic Wave Propagation in Sea Ice

2.2.1 Background

The accurate modeling of seismic wave propagation in floating sea ice is fundamental to infer the ice properties such as its mechanical parameters or its thickness. Within the frequency range of natural sources from the low-frequency hydro-elastic gravity waves generated by swell, to higher-frequency waves generated by impulsive sources such as icequakes, the wavefield recorded on sea ice consists of three fundamental guided wave modes (Moreau et al., 2017):

- the fundamental quasi-symmetric mode (QS0), also called longitudinal wave, with most energy on the radial component of the displacement,
- the quasi-Scholte (QS) mode, also called flexural wave, with most energy on the vertical component of the displacement,
- the fundamental shear-horizontal wave (SH0), with most energy on the transverse component of the displacement

An example of seismic waveforms associated with these three modes is shown in figure 3.

On the theoretical side, considerable effort has been devoted to understand the behavior of guided waves and their various modes of propagation, first in elastic plates in a vacuum (Lamb, 1917), followed by studies involving plates submerged in fluid on one or both sides (e.g., Osborne and Hart, 1945; Press, 1951b). Sea ice represents a particular case within this framework, with the ice layer bounded by air above and water below. Both analytical and asymptotic approaches have been proposed to describe wave behavior under these conditions, along with the development of numerical methods such as finite elements or spectral elements, that account for more complex geometries and boundary conditions.

https://doi.org/10.5194/egusphere-2026-2519
Preprint. Discussion started: 11 June 2026

2.2.2 Leaky Rayleigh–Lamb waves: analytical and thin-plate models

Compared to the classical Lamb wave theory (Lamb, 1917), the boundary conditions at the ice-water interface enforce continuity of normal displacement and normal stress, and vanishing shear stress, which yields a linear system whose coefficients are obtained by applying the fluid–solid boundary conditions at the plate surfaces (Lohne et al., 2008). This approach generalizes the classical Lamb solution for a free plate to fluid-loaded boundaries, allowing radiation of energy into the surrounding media. Solving this system numerically for different wavenumbers and frequencies produces a wavenumber–frequency representation, including the quasi-symmetric and quasi-antisymmetric families, from which the fundamental modes can be extracted. In the following, we refer to this model as the analytical model. While exact in principle, the analytical model is challenging to implement in practice: mode tracking becomes difficult at high frequencies, and it does not easily extend to heterogeneous media.

In the long-wavelength limit ($\lambda \gg h$, where λ is the wavelenght and h the thickness of the plate), the full 3D elastodynamic problem reduces to the classical Kirchhoff-Love thin-plate theory. In thin-plate regime, symmetric and antisymmetric Lamb waves reduce to the fundamental longitudinal and flexural modes, which are no longer coupled. The longitudinal wave is no longer dispersive and propagates at velocity:

$$c_L = \sqrt{\frac{E}{\rho_s(1-\nu^2)}}, \tag{1}$$

where E is the Young's modulus, ρ_s is the solid density, and ν is the Poisson's ratio.

The flexural wave obeys a dispersion relation that incorporates fluid loading and buoyancy. One widely used model for an ice plate floating on water with vacuum above, describing the fundamental flexural–gravity wave, is given by Squire et al. (1996) as

$$\omega^2 = \frac{Dk^4 + g\rho_w}{\rho_i h + \frac{\rho_w}{k}\coth(kH)}, \tag{2}$$

where ρ_i and ρ_w are ice and water densities, g the is gravitational acceleration, H is the water depth, h is the ice plate thickness, k is the wavenumber of the flexural wave, and

$$D = \frac{Eh^3}{12(1-\nu^2)} \tag{3}$$

is the flexural rigidity. Equation 2 represents the propagation of a highly dispersive wave. This dispersion relation is highly sensitive to the ice thickness h due to the cubic dependence of the flexural rigidity D with respect to the thickness h. This makes it a natural candidate for ice thickness reconstruction from seismic data.

The simplicity of the asymptotic solution has made it widely used in many studies. However, its validity is limited to a low frequency-thickness product. This limit appears clearly in Figure 4, around a frequency $\times$ thickness product of 20 Hz·m, where the wavenumber from the asymptotic model starts to diverge from that of the analytical model.

https://doi.org/10.5194/egusphere-2026-2519
Preprint. Discussion started: 11 June 2026

2.2.3 SEM for wave propagation in sea ice sheets

To address the limitation of the analytical and asymptotic models, we adopt a numerical approach based on the Spectral Element Method (SEM). The latter is a state-of-the art method in seismology due to its ability to accurately model seismic wave propagation in complex 2D and 3D heterogeneous media with complex geometries with excellent numerical dispersion properties. SEM employs a mathematical model that is similar to the classical Finite Element Method (FEM), utilizing the weak form of the equation of motion. It combines the flexibility of FEM in handling intricate geometries with the accuracy of pseudospectral methods (Komatitsch and Tromp, 1999; Tromp et al., 2008; Trinh et al., 2019; Cao et al., 2021).

We consider a medium composed of water and ice. In the solid part, we solve the elastic wave equation, while in the fluid part, we solve the acoustic wave equation derived from Euler's and continuity equations, forming a coupled system with continuity of traction at the fluid–solid interface. The governing equations for the coupled ice-water system are:

$$\begin{cases} \frac{1}{\kappa}\ddot{\phi}_f = \nabla\cdot\left(\frac{1}{\rho_f}\nabla\phi_f\right) + \frac{1}{\kappa}P_f \quad \text{in}\Omega_f & \text{Fluid (acoustic)} \\ \rho_s\ddot{\boldsymbol{u}}_s = \nabla\cdot\boldsymbol{\sigma} + \boldsymbol{f}_s, \quad \boldsymbol{\sigma} = \boldsymbol{C}:\boldsymbol{\epsilon} \quad \text{in } \Omega_s & \text{Solid (elastic)} \\ \boldsymbol{u}_s\cdot\boldsymbol{n} = \frac{1}{\rho_f}\nabla\phi_f\cdot\boldsymbol{n}, \quad \boldsymbol{\sigma}_s\cdot\boldsymbol{n} = \ddot{\phi}_f\boldsymbol{n} \quad \text{on } \Gamma_{fs} & \text{Interface conditions} \end{cases} \tag{4}$$

Here ϕ_f is the fluid displacement potential, $\boldsymbol{u}_s$ is the solid displacement vector, $\kappa = \rho_f c_f^2$ is the fluid bulk modulus, $\boldsymbol{C}$ is the fourth-order elasticity tensor, $\boldsymbol{\epsilon} = \frac{1}{2}(\nabla\boldsymbol{u}_s + (\nabla\boldsymbol{u}_s)^T)$ is the strain tensor, P_f and $\boldsymbol{f}_s$ are source terms in fluid and solid, Ω_f and Ω_s are the fluid and solid domains, Γ_{fs} is the fluid-solid interface, and $\boldsymbol{n}$ is the unit normal to the interface.

In this study, we use a 2D SEM code developed for coupled acoustic-elastic wave modeling, derived from the 3D SEM code SEM46 developed in the SEISCOPE research group Trinh et al. (2019); Cao et al. (2022). The free surface boundary condition is implicitly satisfied in SEM, thanks to the integration by part of the weak form of the equation (Komatitsch and Tromp, 1999). However, to generate guided waves in the ice without interference from wave reflections at the model edges, we apply absorbing boundary conditions. This is accomplished by adding absorbing layers that combine a radiative boundary condition (Lysmer and Kuhlemeyer, 1969) and a sponge layer (Cerjan et al., 1985), effectively simulating an infinite domain and avoiding artificial reflections.

2.2.4 Comparison of forward models

To compare the forward models, we evaluate their frequency-wavenumber spectra. Dispersion behavior governs how wave energy propagates in the ice layer, hence comparing frequency-wavenumber dispersion curves is a natural way of comparing the performances of the models. The analytical and thin-plate models are solved numerically to obtain the wavenumber of the flexural wave in a given frequency range. For the spectral element method (SEM), waveforms simulated at multiple receiver locations are converted into the frequency–wavenumber domain via a spatio-temporal Fourier transform of the time-space synthetics. All simulations are performed using a 1 m-thick ice layer, using the mechanical parameters for the ice estimated in March 2019 in the Van Mijen fjord in Svalbard (Table 1).

The comparison is shown in Figure 4, where we also indicate the maximum frequency content of the controlled sources (CS) and natural sources (NS) that are used later in this study. These markers provide context by showing the frequency range in

https://doi.org/10.5194/egusphere-2026-2519
Preprint. Discussion started: 11 June 2026

Table 1. Ice and water properties used in the synthetic database generation for different dates.

Parameter	Symbol	Svalbard (2019)	Canada (2025)
Ice density	ρ_{ice}	$910\,\text{kg/m}^3$	$910\,\text{kg/m}^3$
Ice Poisson's ratio	ν_{ice}	0.27	0.24
Water density	ρ_{w}	$1000\,\text{kg/m}^3$	$1000\,\text{kg/m}^3$
Water sound speed	c_{w}	1480 m/s	1480 m/s
Ice Young's modulus	E	3.8×10^9 Pa	4.9×10^9 Pa

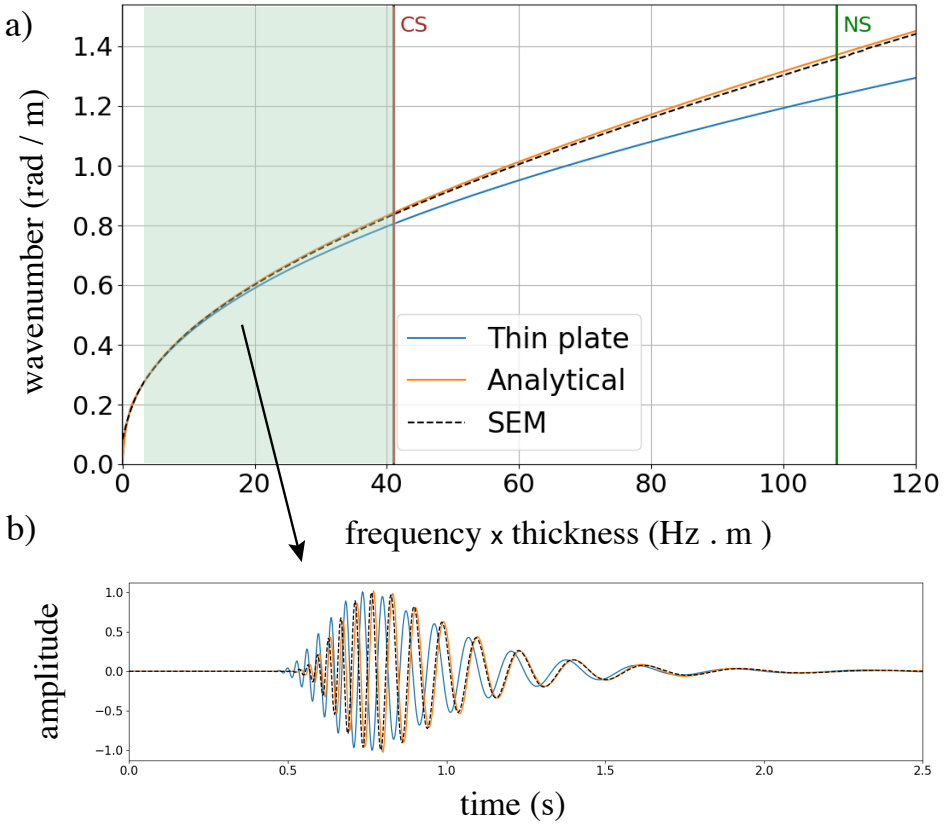

Figure 4. Comparison between the analytical (solid orange line), the thin-plate (solid blue line) and SEM (dotted black line) forward models, in terms of a) frequency-wavenumber dispersion curves and b) waveforms of the flexural wave in a floating ice layer. The waveforms were generated 300 m away from the source, in the frequency band indicated by the green shaded area [5-40]Hz. The vertical lines indicate the maximum frequency content of the waveforms in controlled and natural sources.

https://doi.org/10.5194/egusphere-2026-2519
Preprint. Discussion started: 11 June 2026

the field observations. The results demonstrate that the SEM dispersion curves closely follow the analytical solution across the relevant frequency range, whereas the thin-plate approximation shows increasing deviation at higher frequencies, consistent with its underlying assumptions.

We also compare the three models in terms of waveforms (Figure 4-b). To generate these waveforms, we use a 15-Hz Ricker wavelet, which spans the 5–40 Hz frequency range, typical of waveforms recorded in Canada with CS. While spectral element model computes waveforms, the analytical and thin-plate models yield frequency-dependent wavenumbers. These wavenumbers are converted into waveforms by applying an inverse Fourier transform to the spectra after weighting them by the Ricker wavelet spectrum. The waveforms shown in Figure 4-b, are computed 300 m away from the source. Again, SEM and the analytical solution agree closely in both phase and arrival time, while the thin-plate solution predicts faster arrivals and exhibits noticeable phase mismatch. This discrepancy reflects the simplified physics of the thin-plate model which might directly impact inversion: biased phase velocities lead to systematic errors in inferred thickness.

2.3 Icequake waveform inversion: from data to 2D ice thickness map

2.3.1 Construction of a SEM database

The use of the SEM modeling tool to invert sea-ice data is appealing due to its better accuracy compared to the asymptotic model in the higher end of the frequency spectrum. However, this goes in hand with a significantly increased computational cost, which would make stochastic inversion used in this study intractable.

To remedy this issue, we build ”offline” a database of seismic waveform which we parameterize using the source-receiver distance and the ice thickness. We discretize these two parameters using x m interval for the source-receiver distance and y cm interval for the ice thickness, spanning distances from 0 to xx m and ice thicknesses from 0 to yy cm. This results in the computation of z waveforms constituting our SEM database, which we perform on the local computing facilities of the Univ. Grenoble Alpes. The source-time function used for this simulation is calibrated to cover the frequency range of the actual seismic data. The ice mechanical parameters we use are taken from (Kuchly et al., 2026) and are presented in Table 1.

2.3.2 Joint estimation of the source position and the thickness estimation along source-receiver paths

We assume events have been detected and separated to constitute a first catalog of icequakes. Our strategy is inspired by Moreau et al. (2023) and is decomposed in three main steps summarized in Algorithm 1 (steps 2-4).

In step 1, we perform a simultaneous inversion of the icequake position (latitude and longitude) and ice thickness using a stochastic approach, namely simulated annealing (Ingber, 1992, 1993; Sen and Stoffa, 2013), assuming the same ice thickness along all the source-receiver paths. Although three geophones are theoretically sufficient to triangulate the icequake coordinates, Moreau et al. (2023) show that using five station improves accuracy, owing to a larger spatial aperture, while keeping the computational cost low.

https://doi.org/10.5194/egusphere-2026-2519
Preprint. Discussion started: 11 June 2026

Because waveform dispersion depends on both ice thickness and propagation distance, enforcing a uniform thickness along the five icequake-geophone paths introduces bias in both the inferred source position and ice thickness. To reduce this bias, we refine the thickness estimation in a second step, which allows path-dependent thicknesses. Starting from positions and thicknesses found in the first step, we perform an additional simulated annealing inversion jointly optimizing the icequake position and individual path thicknesses. This is what we call the position refinement step.

Finally, in step three, from the improved icequake positions, we perform a final grid search to update only the ice thicknesses along individual wave path from source to all receivers of the array. This is what we call the thickness refinement step.

At each stage of the algorithm, we minimize a misfit measured between synthetic and field data which can be formulated as

$$\text{misfit} = \frac{1}{N}\sum_{n=1}^{N}\left[1 - R_0\left(D_{syn}^{(n)}, D_{obs}^{(n)}\right)\right], \tag{5}$$

where $D_{syn}^{(n)}$ and $D_{obs}^{(n)}$ are the synthetic and observed data at receiver n, respectively. The quantity R_0 denotes the normalized zero-lag correlation, which we compute in the frequency domain for efficiency:

$$R_0^{(n)} = \frac{\int_\Omega D_{syn}^{(n)}(\omega)\, D_{obs}^{(n)*}(\omega)\, d\omega}{\sqrt{\left(\int_\Omega |D_{syn}^{(n)}(\omega)|^2 d\omega\right)\left(\int_\Omega |D_{obs}^{(n)}(\omega)|^2 d\omega\right)}}. \tag{6}$$

In this equation, the star symbol indicates complex conjugate.

2.3.3 Thickness Tomography

From the ice thickness estimates retrieved along source–receiver paths we want to generate a 2D ice-thickness map. To do this we use a method similar to what is used for travel-time tomography with straight rays (see for instance Nolet, 2008, for an overview of seismic tomography techniques).

Each observation, i, represents a path-averaged ice thickness estimated along a source-receiver path. Physically, this corresponds to integrating the local ice-thickness field, $h(x,y)$, along the ray path L_i, and then normalizing by the total path length:

$$h_{\text{obs},i} = \frac{1}{L_i}\int_{L_i} h(x,y)\,\mathrm{d}\ell. \tag{7}$$

We discretize the domain into $N = N_x \times N_y$ cells, with N_x and N_y the number of cells in the x- and y-directions, respectively. We assume a constant ice-thickness value h_j in each cell, for $j = 1, \ldots, N$. In this setting, the integral (7) can be approximated as the weighted sum

$$h_{\text{obs},i} = \sum_{j=1}^{N} w_{ij} h_j, \tag{8}$$

https://doi.org/10.5194/egusphere-2026-2519
Preprint. Discussion started: 11 June 2026

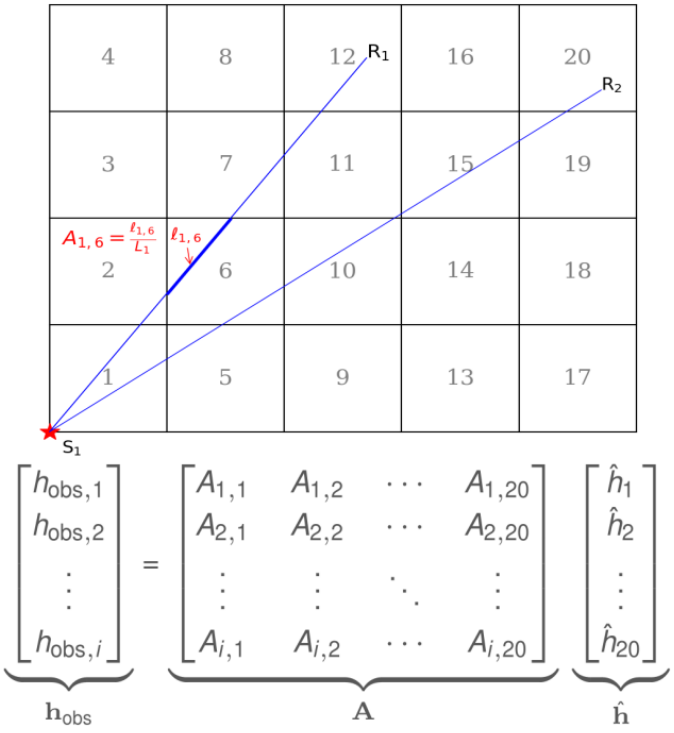

Figure 5. Top: Example 4×5 cell grid showing two ray paths from source S_1 to receivers R_1 and R_2. Bottom: Corresponding matrix form.

where $w_{ij} = \frac{\ell_{ij}}{L_i}$ represents the normalized contribution of the cell j to the path i, i.e., the fraction of the total ray length that crosses that cell. In matrix form, this discrete relationship can be compactly written as

$$\mathbf{h}_{\text{obs}} = \mathbf{A}\mathbf{h}. \tag{9}$$

The vector $\mathbf{h}$ has dimensions N, while $\mathbf{h}_{\text{obs}}$ has dimension N_{path}, corresponding to the number of source–receiver paths. The rectangular matrix $\mathbf{A}$ with N_{path} rows and N columns collects all the weights w_{ij}. Each row of $\mathbf{A}$ corresponds to one ray path and represents a normalized linear averaging operator over the intersected cells. A schematic example how the system (9) is built is presented in Figure 5.

In practice we expect to have an overdetermined linear system (for a sufficient number of sources and receivers). We look for a least-squares solution of this system, and introduce Tikhonov regularization to mitigate the ill-determination associated with poorly sampled cells. We therefore compute a solution of the problem

$$\min_{\mathbf{h}} \|\mathbf{W}_d(\mathbf{A}\mathbf{h} - \mathbf{h}_{\text{obs}})\|_2^2 + \alpha^2 \|\mathbf{W}_m(\mathbf{h} - \mathbf{h}_{\text{prior}})\|_2^2 + \beta^2 \|\mathbf{L}\mathbf{h}\|_2^2, \tag{10}$$

where $\mathbf{W}_d$ is a data-covariance weighting matrix, $\mathbf{W}_m$ is a model-covariance weighting matrix, $\mathbf{h}_{\text{prior}}$ is a prior model for the 2D ice thickness map, $\mathbf{L}$ is a linear operator associated with the first-order finite-difference approximation of the spatial gradient, α and β are weighting parameters. The first term of the functional in equation (10) is thus a data misfit term, the

https://doi.org/10.5194/egusphere-2026-2519
Preprint. Discussion started: 11 June 2026

second term a prior information term, while the third term promotes models with small spatial variation, hence a smoothing term.

The solution $\overline{\mathbf{h}}$ of equation (10) is found by finding the zero of misfit function gradient, which yields

$$\overline{\mathbf{h}} = \mathbf{M}^{-1}\mathbf{b} \tag{11}$$

where

$$\mathbf{M} = \mathbf{A}^T\mathbf{W}_d^T\mathbf{W}_d\mathbf{A} + \alpha^2\mathbf{W}_m^T\mathbf{W}_m + \beta^2\mathbf{L}^T\mathbf{L}, \tag{12}$$

and

$$\mathbf{b} = \mathbf{A}^T\mathbf{W}_d^T\mathbf{h}_{\text{obs}} + \alpha^2\mathbf{W}_m^T\mathbf{W}_m\mathbf{h}_{\text{prior}}. \tag{13}$$

Equations (11) to (13) give the general form of the solution. In practice, in the applications presented in the next Section we assume independent data with same variance, which consists in setting the data-covariance matrix $\mathbf{W}_d$ as the identity : $\mathbf{W}_d = \mathbf{I}$. We will assume the same for the model-covariance matrix $\mathbf{W}_m = \mathbf{I}$. Finally, since the medium is 2D, the operator L can be rewritten as

$$\mathbf{L} = \begin{pmatrix} \mathbf{D}_x \\ \mathbf{D}_y \end{pmatrix}, \tag{14}$$

where D_x and D_y denote first-order discretization of the spatial partial derivative operator ∂x and ∂y respectively. Therefore, the operator $\mathbf{L}^T\mathbf{L}$ in the matrix $\mathbf{M}$ corresponds to

$$\mathbf{L}^T\mathbf{L} = \mathbf{D}_x^T\mathbf{D}_x + \mathbf{D}_y^T\mathbf{D}_y \tag{15}$$

in which we recognize a discrete version of the Laplacian operator. The smoothing term thus induces an (inverse) Laplacian smoothing contribution in the solution matrix $\mathbf{M}^{-1}$, which is associated with conventional Gaussian smoothing through linear diffusion (see for instance Weickert, 1998).

The regularization parameters, α and β, can be determined using L-curve analysis. Another, more practical method for tuning these parameters is to perform some checkerboard tests. Those tests offer a practical way to assess the resolving power of the inversion under realistic conditions. In this approach, a synthetic model with alternating high and low values is constructed, and noise-free data are generated using the same acquisition geometry, model parameterization, and forward operator as the real experiment. The inversion is then performed with the same algorithm and regularization settings as for the real experiment. Comparing the recovered model to the input checkerboard pattern highlights where anomalies are well-resolved and where smearing or loss of resolution occurs, providing an intuitive and visual assessment of the inversion capabilities.

In the following examples, tomography inversions of field data are presented. For each case, a checkerboard test has been conducted, and regularization parameters have been determined through trial and error.

https://doi.org/10.5194/egusphere-2026-2519
Preprint. Discussion started: 11 June 2026

2.3.4 Summary of the inversion method

We summarize the inversion method we set up in the 5 stages Algorithm 1.

Algorithm 1 Icequake data inversion: generating 2D maps of ice thickness .

1 : Generate a SEM data base considering difference source-receiver distances and ice thicknesses along the wave path
2 : Invert for source position and **same** ice thickness for **the five** source-receiver wave path with simulated annealing
3 : Invert for source position and ice thickness for **each** source-receiver wave path with simulated annealing
4 : Refine the ice thickness for **each** source-receiver wave path using a gridsearch approach
5 : Spatialize the ice thickness along the wave path in a 2D map using a tomography-like approach

3 Results

3.1 Inversion icequake data from controlled sources in Canada

When the source position is known, steps 2 and 3 of Algorithm 1 are not necessary and then skipped. For the Canada data experiment we thus move directly from step 1 to step 4. When performing step 4 (refinement of the ice thickness along each wave path), we found that part of the dataset was of poor quality, either exhibiting a low signal-to-noise ratio (SNR) or showing scattering patterns. This can be due to several factors, the most common being inconsistent source generation or the presence of large cracks in the ice along the propagation path, which prevent the flexural wave from reaching some geophones with sufficient amplitude. In such cases, the misift was not low enough for the inversion to be meaningful. In order to have a good compromise between the number of source-receiver rays and inversion quality, we defined a heuristic threshold of 0.3 as the maximum acceptable misfit to keep an inverted thickness value along a source-receiver path. An example of the fit is shown in Figure 6.

The result of this grid search is shown in Figure 7. 296 rays were selected amongst the 528 sources-receivers paths (56%). The distribution of thicknesses on the rays seem to indicate a dichotomy with larger thicknesses to the left and smaller thicknesses to the right, which is consistent with field observations and thickness values obtained from drillings (Figure 1).

The tomographic inversion applied to the dataset with controlled sources is shown in Figure 8-a. It was obtained using a regular mesh of $2\,\mathrm{m} \times 2\,\mathrm{m}$ cells, with the parameter $\beta = 0.12 - 0.15$ selected through trial and error (here $\alpha = 0$, since only we did not have any reliable prior model to guide the inversion here. The tomography clearly reveals the transition from thicker to thinner ice across the array, consistent with the observed ice ridge separating the two ice types in the field.

Figure 8-b shows the ice thickness along a cross section of the tomography to compare it with the thickness values inferred from frequency-wavenumber spectra of the flexural wave recorded using a fiber optic cable and a DAS interrogator (Kuchly et al., 2026). The agreement between the two sets of thickness estimations is striking. It is noteworthy that both methods reproduce the thickness discontinuity with very good spatial resolution, but values are consistantly about 5 cm lower than the thickness values from drillings. We attribute this bias to the fact that, at the bottom, the ice is composed of porous, consolidated

https://doi.org/10.5194/egusphere-2026-2519
Preprint. Discussion started: 11 June 2026

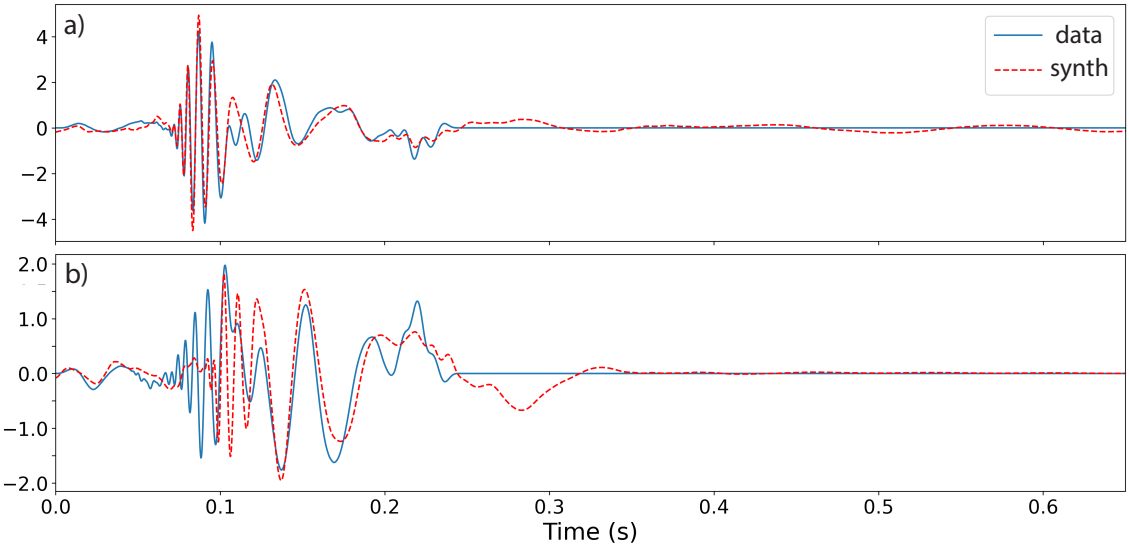

Figure 6. Examples of waveform fits between observed and synthetic data: a) misfit value of 0.125, and b) poorer fit with a misfit value of 0.31

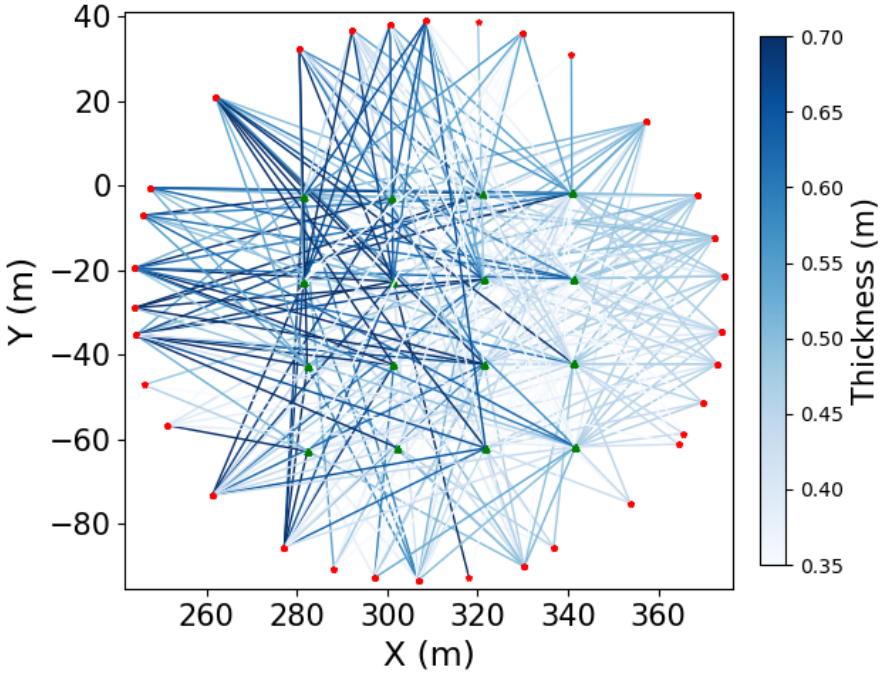

Figure 7. Selected paths (296) amongst the 33 sources and 16 receivers.

https://doi.org/10.5194/egusphere-2026-2519
Preprint. Discussion started: 11 June 2026

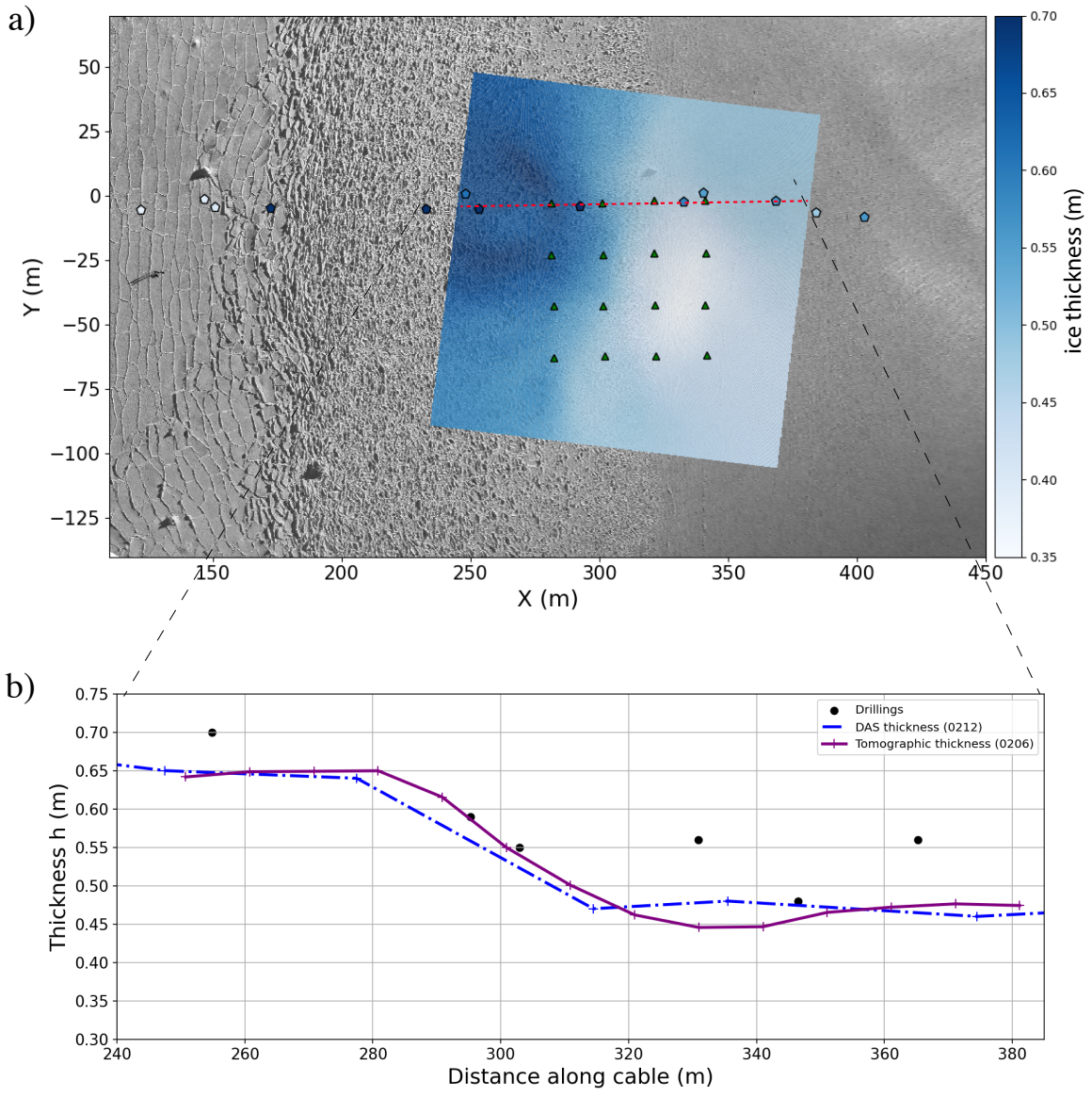

Figure 8. a) Results of the tomographic inversion of the controlled data recorded in Canada. a) 2D map of the ice thickness and b) Cross-section of the tomography along the red dotted line (purple solid line), for comparison with thicknesses from Kuchly et al. (2026), obtained on 10 February by inverting Distributed Acoustic Sensing seismic data (dotted blue line) and drillings (filled circles).

slush, which is significantly softer than the upper layer. While too soft to guide the flexural wave, this layer is stiff enough to halt the measuring tape hook.

https://doi.org/10.5194/egusphere-2026-2519
Preprint. Discussion started: 11 June 2026

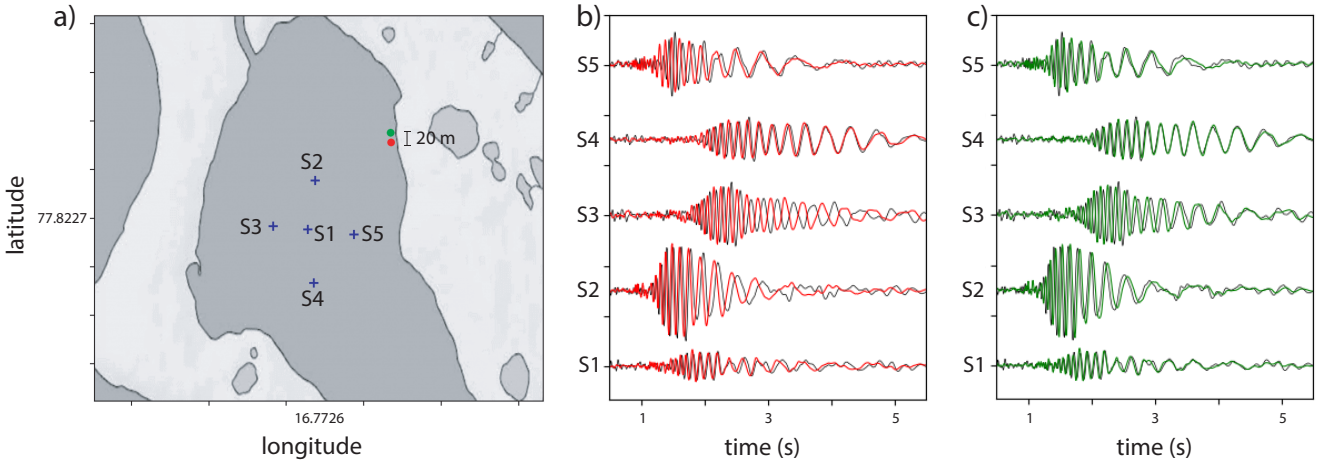

Figure 9. Comparison between a) the position of a relocated icequake and b),c)the inverted waveforms for the method in Moreau et al. (2023) (red) and the method described in section 2.3.2 (green).

3.2 Inverting icequake data from natural sources in Svalbard

For this experiment in Svalbard with the recording of natural icequakes, we apply the full workflow depicted in Algorithm 1. We first illustrate the effect of step 3 (source location refinement). In this framework, the source location search is restricted to a square area of side length ± 25 m around the location obtained in step 2 and constrained to lie within the fjord shoreline. Simultaneously, thicknesses along each path to the five geophones are allowed to vary by ± 15 cm around the catalog value. Although the refined search could be extended to a larger solution space, we consider this unnecessary because the initial solution is assumed to be close enough to the global optimum. Compared to the original source location, the misfit in the new source location and ice thickness is reduced by a factor between 20–30%, depending on icequakes. Figure 9 illustrates this improvement by comparing inverted waveforms to field data for the old and improved source locations/ice thicknesses. Nonetheless, similarly to the dataset from Canada with controlled sources, we apply a quality check to the inversion, by keeping only those where the misfit is less than 10%. This value is smaller than the value used for the Canada experiment. This is because the ice in Svalbard was more continuous and with less cracks, resulting in overall cleaner waveforms. Figure 10 shows the total number of source-receiver paths per day and the number of paths kept for tomography. The resulting catalog contains more than 5300 icequakes recorded between 28 February and 24 March 2019. The vast majority of icequake sources are located along the shoreline (see the ray paths shown in figure 12 for different days of March 2019), where mechanical stress accumulates due to tidal forcing. The number of icequakes detected each day varies from a few hundred at the beginning of March to around 50 in mid-March, before increasing slightly again after 20^{th} March.

Instead of applying our strategy to generate a single 2D map of ice thickness, the large period of deployment and the high number of detected icequakes per day makes it possible to cluster the different icequakes per day and build 2D ice thickness maps for each day of the acquisition. In this setting, the ice thickness map built from one day serve as a prior model $\mathbf{h}_{\text{prior}}$ to

https://doi.org/10.5194/egusphere-2026-2519
Preprint. Discussion started: 11 June 2026

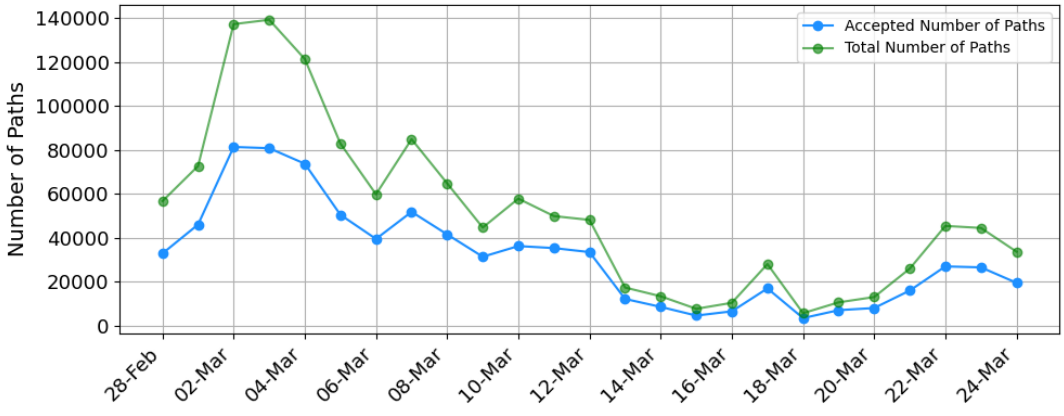

Figure 10. Number of source–receiver paths before and after filtering based on cost value.

constrain the inversion on the next day. In order to incorporate the previous day's model as a prior, one must account for the fact that ray coverage varies across cells. To address this, different weights are assigned to each cell based on ray coverage. Here the matrix $\mathbf{W}_m = \mathbf{C}_m^{-1/2} \neq \mathbf{I}$, and the corresponding cell weights are assigned based on the local ray-path density: cells with no coverage or reduced coverage relative to the previous day receive a small weight (here 0.01), cells with equal or higher coverage receive a weight of 1, and intermediate cases are weighted by the ratio of current-to-previous ray counts.

The daily 2D maps we generate are based on a a regular mesh with a spacing of $6\ \mathrm{m} \times 6\ \mathrm{m}$. This cell size is small enough to produce smooth and spatially detailed ice thickness maps while remaining consistent with the resolution power of our dataset, making finer discretization unnecessary. The mesh is shown in Figure 11. The survey area displayed here covers approximately $900\ \mathrm{m} \times 1,200\ \mathrm{m}$.

The resulting tomographies are shown in Figure 13, for three dates: 1, 12, and 24 March 2019. A key observation is the non-uniform ice thickness across the area, in particular with a larger thickness along the shore. This variability is influenced by both the shore geometry and local hydrodynamic processes. As discussed by Marchenko et al. (2021), ice near the shoreline tends to grow thicker due to shallower water depths, which inhibit convection and reduce heat transfer from the water column to the ice base. Moreover, between the beginning and the end of the deployment, we note an overall ice thickness increase of about 10–15 cm. This trend is also clearly visible in the complete evolution of daily ice-thickness tomographic reconstructions shown in Figure A-1 of Annex A. Field measurements reported by Marchenko et al. (2021) indicate ice thicknesses of 75–80 cm near the northern channel around mid-March, which are successfully captured by our inversion.

To validate our results, we compare them with those of Serripierri et al. (2022), which were estimated from noise interferometry and frequency–wavenumber spectrum inversions. These estimates were obtained along two orthogonal lines within the area containing the dense array of geophones, a square zone with a side length of 50 m. Therefore, we calculated the average ice thickness within this area from 28 February to 24 March and plotted the results in Figure 14. Both sets of inversions exhibit a similar increase in ice thickness, on the order of 10–15 cm. However, whereas the inversions of Serripierri et al. (2022) show

https://doi.org/10.5194/egusphere-2026-2519
Preprint. Discussion started: 11 June 2026

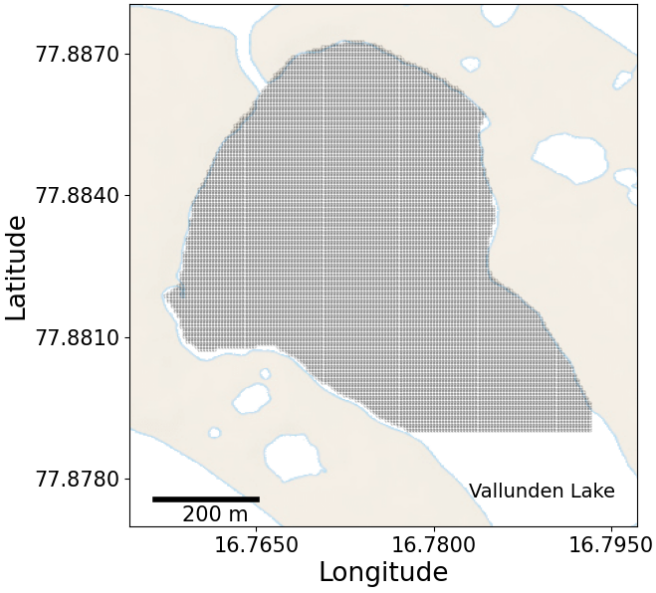

Figure 11. Regular $6\ \mathrm{m} \times 6\ \mathrm{m}$ mesh used in the tomography.

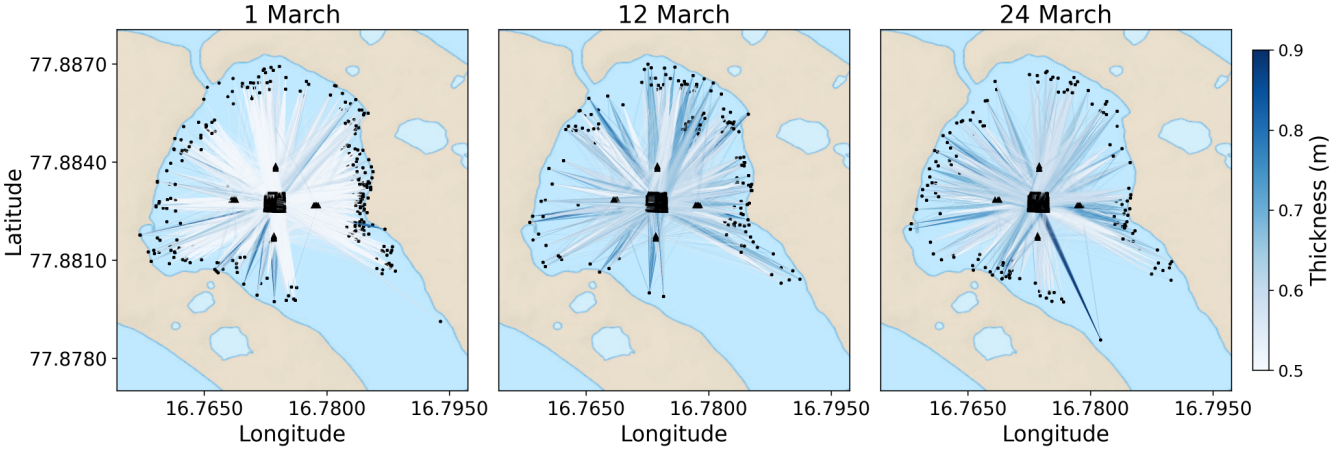

Figure 12. Ray paths and corresponding thicknesses between icequakes location and the geophones on three days of March 2019.

https://doi.org/10.5194/egusphere-2026-2519
Preprint. Discussion started: 11 June 2026

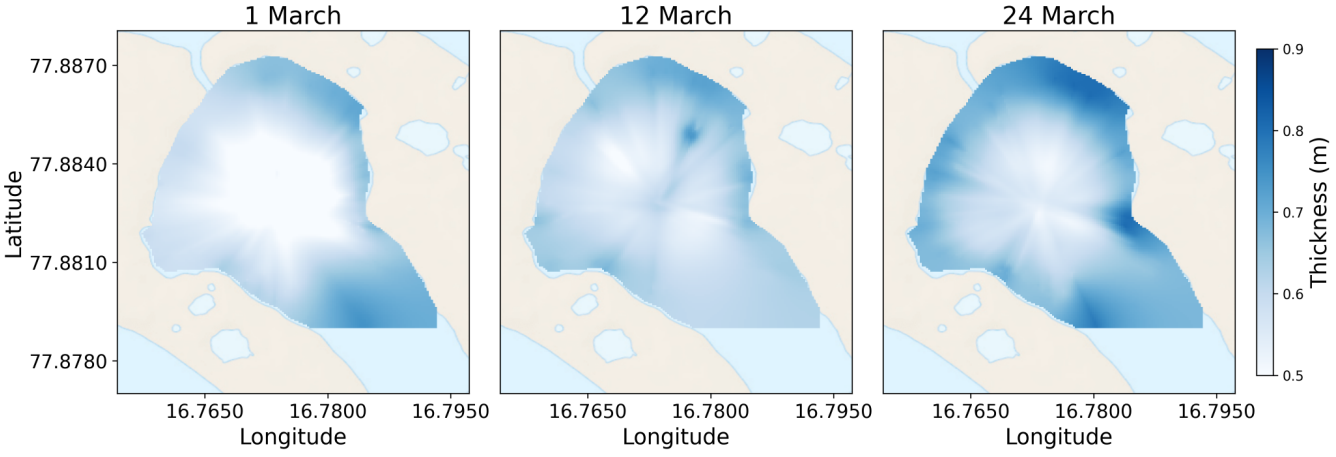

Figure 13. Results of the tomographic inversion of the passive data recorded in Svalbard, on three days of March 2019.

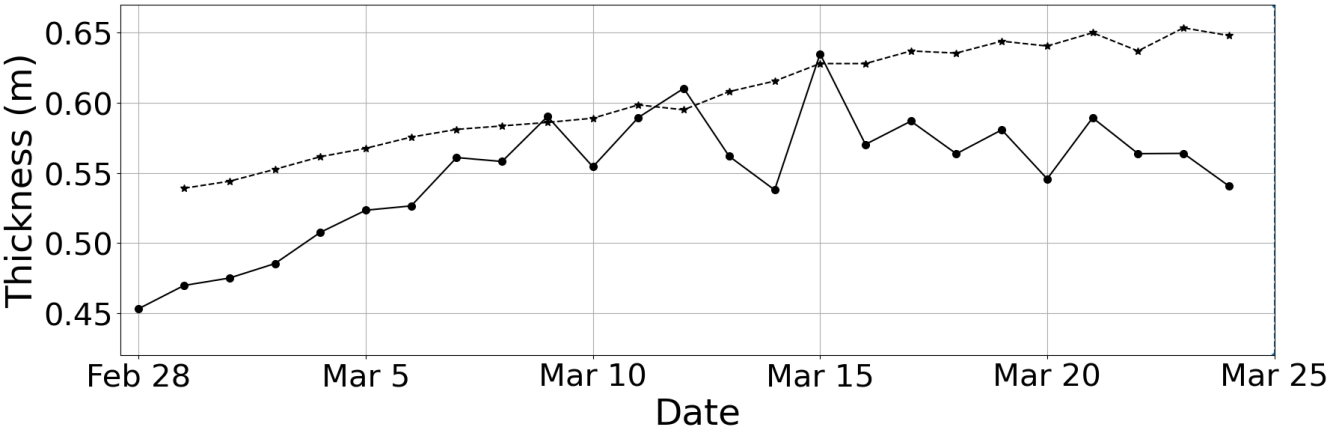

Figure 14. Evolution of ice thickness in the dense array area. The dashed line shows results from Serripierri et al. (2022) in the dense array. The solid black line represents the average ice thickness from our tomography results across all cells in this region.

https://doi.org/10.5194/egusphere-2026-2519
Preprint. Discussion started: 11 June 2026

a relatively steady growth, the tomography reveals a sharp increase during the first half of March, followed by a stabilization in the second half. This trend is consistent with the temperature evolution. Early March was characterized by particularly low surface temperatures, when values dropped below $-30°C$, promoting active ice growth. In contrast, temperatures rose to near 0°C during the second half of March. The differences in absolute values and temporal trends between the two methods are discussed in section 4.

Ice drillings near the central geophones gave ice thickness between 62 cm on 1 March and 70-73 cm on 26 March, confirming the same order of thickness growth. However both methodologies indicate thickness values lower than drillings. Similarly to the tomography from controlled sources in Canada (section 3.1), we attribute this bias to the fact that the ice is not homogeneous through the thickness. In Canada, the ice was very soft and barely consolidated at the bottom. In Svalbard the ice was quite hard at the bottom (no slush, because there was neither gravity waves nor strong currents), but very porous in the top 10-15 cm, including compacted snow. This soft layer modifies the flexural wave velocity, resulting in a lower apparent thickness.

4 Discussion

The method introduced in this paper appears very promising for 3D mapping of sea ice thickness. However, some questions remain regarding its limitations and potential improvements. For the dataset recorded in Canada with controlled sources, the thickness estimates obtained from tomographic inversions are consistent with those derived from frequency–wavenumber spectrum inversions, suggesting that both methods yield comparable results under controlled acquisition conditions.

In contrast, for the dataset recorded in Svalbard with natural sources, the two methods produce slightly different thickness estimates. However, in Serripierri et al. (2022), frequency–wavenumber spectrum inversions were applied to seismic noise correlations rather than to direct measurements of seismic waveforms, as in the Canadian dataset. This difference in the nature of the data suggests that the observed discrepancy is less likely to arise from the inversion methods themselves, and may instead be related to additional averaging effects inherent to noise-based measurements.

On the one hand, the spatial Fourier transform is not sensitive to local variations, as it averages the data over a distance of approximately 50 m. On the other hand, noise interferometry relies on correlations of seismic data recorded over several hours at pairs of geophones, integrating contributions from icequakes and other seismic sources. As a result, the correlation process introduces additional averaging effects, both over time and over the distances between sensor pairs (less than 150 m). In other words, the estimates of Serripierri et al. (2022) represent a temporally and spatially smoothed version of the ice-thickness evolution along short baselines. This smoothing could explain the difference in the observed trends, with one dataset showing a more gradual evolution and the other exhibiting sharper variations followed by stabilization.

Moreover, the accuracy of the tomographic inversion depends on the density of ray paths crossing each cell, which in this case is controlled by the number and spatial distribution of icequakes. These vary substantially from one day to the next. Although this impact is mitigated by incorporating prior information from the previous day, it may still affect the quality of the estimated thickness. Denser ray distributions, as well as broader and more uniform spatial coverage, result in more accurate thickness estimates. It is therefore likely that, with additional sources near the dense array, the difference between the two

https://doi.org/10.5194/egusphere-2026-2519
Preprint. Discussion started: 11 June 2026

methods would vanish, as observed for the Canada dataset, where sources are distributed all around and close to the geophone array. A possible way to investigate this further would be to perform a tomography from the noise correlations between all pairs of geophones, drastically increasing the ray density and spacial coverage in the dense array. However this is out of the scope of this paper, and we are mainly interested in showing the potential for larger scale ($\mathcal{O}$(1 km)) thickness estimations, not only small scale ($\mathcal{O}$(50 m)).

Potential improvements to our approach could involve exploring other types of cost functions. The use of cross-correlations of signals is known to be non-convex, owing to the oscillatory behavior of the waveforms. Alternative misfit functions, for example those based on spectrogram correlations or on optimal transport distances (**?**), could improve the convergence of the inversion in steps 2–4 of the procedure.

For larger-scale tomographies, using a regular mesh could become prohibitive in terms of computational cost. To address this issue, we suggest that an adaptive mesh, in which the cell size is driven by ray density, could substantially reduce the computational load by using larger cells where ray density is low and smaller cells where it is high. For this approach to be successful, further developments are required to compute the spatial gradient in the operator $\mathbf{L}$ of Eq. (10).

Finally, extending the database with a varying Young's modulus could open the possibility to produce simultaneous maps of the ice thickness and rigidity, by exploiting waveforms from the non-dispersive modes on the horizontal channels. Young's modulus is a key parameter for sea ice models, which currently assume a constant value, while field observation show important variations between 1 and 9 GPa (Moreau et al., 2020a; Kuchly et al., 2025), with significant impact on the response of sea ice to geophysical forcing in the marginal ice zone.

https://doi.org/10.5194/egusphere-2026-2519
Preprint. Discussion started: 11 June 2026

5 Data availability

The dataset for the experiment in Canada is available at https://doi.org/10.57745/D3CJYO. The dataset for the experiment in Svalbard (Norway) is available at https://doi.org/10.15778/RESIF.XG2019

6 Code availability

The codes used to post-process the data are available at https://github.com/Turbotice/icewave.git This repository provides more than the code required to post-process and analyze the dataset introduced in the manuscript. In particular, we use it to process the data acquired during the BicWin campaign every year, as well as to analyze experimental data at the laboratory scale.

It should be noted that this repository is made available for open science purposes, but it is not made to be a tutorial for processing the data. A user guide is in development, but not yet available. In case of difficulties in extracting the scripts, please contact the authors with your inquiries.

7 Conclusion

This study presents a seismic framework for reconstructing sea ice thickness that combines waveform inversion with tomography, using controlled or natural seismic sources. Applications to field data from the St. Lawrence Estuary (Canada) and Van Mijen Fjord (Svalbard) demonstrate that the approach is robust across different environments and acquisition strategies, and capable of resolving both spatial variability and temporal evolution of ice thickness.

By relying on forward modeling of wave propagation in a floating ice–water system, the method provides reliable path-averaged thickness estimates that can be directly integrated into a tomographic inversion. In the controlled-source experiment, the resulting thickness map reproduces sharp lateral contrasts and agree well with independent drilling and DAS-based estimates. In the passive experiment, the use of icequakes as natural sources enables daily tomographic reconstructions over a 25-day period, capturing temporal thickness trends and persistent spatial patterns, including thicker ice near shorelines and thinner ice in the central regions.

These results show that passive-source seismic tomography can provide spatially resolved, time-dependent maps of ice thickness. The method therefore offers a complementary tool to existing in situ and remote-sensing techniques, particularly in environments where access is limited and continuous monitoring is needed, reinforcing its potential as a reliable tool for long-term monitoring of sea ice evolution in the Arctic.

Future developments may focus on extending the forward and inverse frameworks to account for more complex ice conditions, such as heterogeneity, anisotropy, or snow cover, and on jointly inverting for additional mechanical properties. More broadly, this work highlights the potential of seismic observations for long-term monitoring of sea ice evolution and for improving our understanding of cryospheric processes in a changing climate.

https://doi.org/10.5194/egusphere-2026-2519
Preprint. Discussion started: 11 June 2026

Appendix A: Daily Ice-Thickness Tomography for the Svalbard Dataset

This appendix presents the complete set of daily ice-thickness tomographic reconstructions for the Svalbard dataset, covering the period from 28 February to 24 March 2019.

Author contributions. HZ produced the methodological developments used in this paper. LMo organized, quality-controlled, processed, and analyzed the two datasets, and is the PI of the two ANR projects that funded this research. LMe and RB developed the SEM46 code. LMo, LMe, and RB supervised the methodological developments. SK, VZ, NM, VD, SP, AE, and DD collected the field data in Canada.

Competing interests. The authors declare that they have no competing interests.

Acknowledgements. This study was partially funded by the Agence Nationale de la Recherche with projects *Multiscale monitoring of sea ice parameters with passive seismology and deep learning*, grant no. ANR-23-CE01-0020, and *Icewaveguide*, grant no. ANR-17-CE01-0019, and by the SEISCOPE consortium (*http://seiscope2.osug.fr*), sponsored by Aker BP, DUG, EXXONMOBIL, GEOLINKS, JGI, PETROBRAS, SHEARWATER, SHELL, TOTALENERGIES and VIRIDIEN. This study was granted access to the HPC resources provided by the GRICAD infrastructure (https://gricad.univ-grenoble-alpes.fr), which is supported by Grenoble research communities, the HPC resources of Cray Marketing Partner Network (https://partners.cray.com), and those of CINES/IDRIS/TGCC under the allocation 046091 made by GENCI.

https://doi.org/10.5194/egusphere-2026-2519
Preprint. Discussion started: 11 June 2026

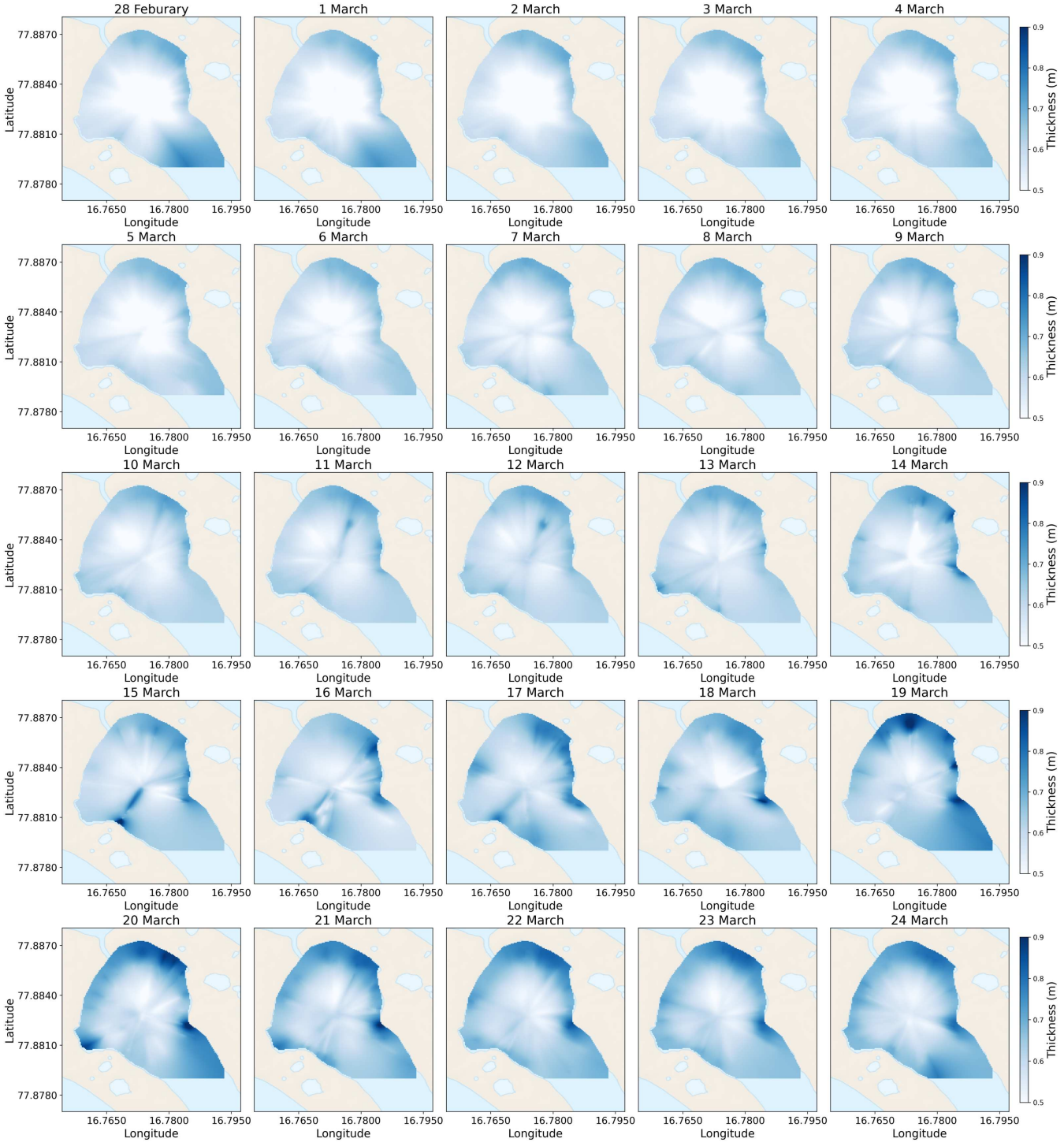

Figure A-1. Daily ice-thickness tomographic reconstructions for the Svalbard dataset.

https://doi.org/10.5194/egusphere-2026-2519
Preprint. Discussion started: 11 June 2026

References

Ardyna, M., Babin, M., Gosselin, M., Devred, E., Rainville, L., and Tremblay, J.-É.: Recent Arctic Ocean sea ice loss triggers novel fall phytoplankton blooms, Geophysical Research Letters, 41, 6207–6212, https://doi.org/https://doi.org/10.1002/2014GL061047, 2014.

Cao, J., Brossier, R., Górszczyk, A., Métivier, L., and Virieux, J.: 3-D multiparameter full-waveform inversion for ocean-bottom seismic data using an efficient fluid–solid coupled spectral-element solver, Geophys. J. Int., 229, 671–703, https://doi.org/10.1093/gji/ggab484, 2021.

Cao, J., Brossier, R., Górszczyk, A., Métivier, L., and Virieux, J.: 3D multi-parameter full-waveform inversion for ocean-bottom seismic data using an efficient fluid-solid coupled spectral-element solver, Geophysical Journal International, 229, 671–703, 2022.

Cerjan, C., Kosloff, D., Kosloff, R., and Reshef, M.: A Nonreflecting boundary-condition for discrete acoustic and elastic wave-equations, Geophysics, 50, 705–708, https://doi.org/10.1190/1.1441945, 1985.

Comiso, J. C., Meier, W. N., and Gersten, R.: Variability and trends in the Arctic Sea ice cover: Results from different techniques, Journal of Geophysical Research: Oceans, 122, 6883–6900, https://doi.org/https://doi.org/10.1002/2017JC012768, 2017.

Ewing, M. and Crary, A. P.: Propagation of Elastic Waves in Ice. Part II, Physics, 5, 181–184, https://doi.org/10.1063/1.1745249, 1934.

Ewing, M., Crary, A. P., and Thorne, A. M.: Propagation of Elastic Waves in Ice. Part I, Physics, 5, 165–168, https://doi.org/10.1063/1.1745245, 1934.

Fissel, D., Marko, J., and Melling, H.: Advances in upward looking sonar technology for studying the processes of change in Arctic Ocean ice climate, Journal of Operational Oceanography, 1, 9–18, https://doi.org/10.1080/1755876X.2008.11081884, 2008.

Ford, J. D., Pearce, T., Canosa, I. V., and Harper, S.: The rapidly changing Arctic and its societal implications, WIREs Climate Change, 12, e735, https://doi.org/https://doi.org/10.1002/wcc.735, 2021.

Hunkins, K.: Seismic studies of sea ice, Journal of Geophysical Research, 65, 3459–3472, https://doi.org/10.1029/JZ065i010p03459, 1960.

Ingber, L.: Very Fast simulated re-annealing, Mathematical and Computer Modelling, 12, 967–973, 1992.

Ingber, L.: Simulated annealing: Practice versus theory, Mathematical and Computer Modelling, 18, 29–57, https://doi.org/https://doi.org/10.1016/0895-7177(93)90204-C, 1993.

Johansen, T. A., Ruud, B. O., and Hope, G.: Seismic on floating ice on shallow water: Observations and modeling of guided wave modes, GEOPHYSICS, 84, P1–P13, https://doi.org/10.1190/geo2018-0211.1, 2019.

Kim, Y.-H., Min, S.-K., Gillett, N. P., Notz, D., and Malinina, E.: Observationally-constrained projections of an ice-free Arctic even under a low emission scenario, Nature Communications, 14, 3139, https://doi.org/10.1038/s41467-023-38511-8, 2023.

Komatitsch, D. and Tromp, J.: Introduction to the spectral element method for three-dimensional seismic wave propagation, Geophys. J. Int., 139, 806–822, https://doi.org/10.1046/j.1365-246x.1999.00967.x, 1999.

Kuchly, S., Auvity, B., Mokus, N., Bureau, M., Nicot, P., Fourgeaud, A., Dansereau, V., Eddi, A., Perrard, S., Dumont, D., and Moreau, L.: An integrated multi-instrument methodology for studying marginal ice zone dynamics and wave-ice interactions, EGUsphere, 2025, 1–23, https://doi.org/10.5194/egusphere-2025-3304, 2025.

Kuchly, S., Moreau, L., Zanchi, V., Mokus, N., Dansereau, V., Smith, M. M., Dumont, D., Perrard, S., and Eddi, A.: High-Resolution Measurement of Sea Ice Mechanical Characteristics Using Distributed Acoustic Sensing, Seismological Research Letters, (under review), 2026.

Lamb, H.: On Waves in an Elastic Plate, Proceedings of the Royal Society of London. Series A, Containing Papers of a Mathematical and Physical Character, 93, 114–128, http://www.jstor.org/stable/93792, 1917.

https://doi.org/10.5194/egusphere-2026-2519
Preprint. Discussion started: 11 June 2026

Landschulze, M.: Seismic wave propagation in floating ice sheets – a comparison of numerical approaches and forward modelling, Near Surface Geophysics, 16, 493–505, https://doi.org/https://doi.org/10.1002/nsg.12013, 2018.

Lohne, K. D., Lunde, P., and Vestrheim, M.: Ultrasonic signal transmission in plates – Study of a steel plate immersed in water, 2008.

Lysmer, J. and Kuhlemeyer, R.: Finite Dynamic Model for Infinite Media, J Eng Mech, ASCE, 95, https://doi.org/10.1061/JMCEA3.0001144, 1969.

Mäkynen, M., Jari, H., Giuseppe, A., Beena, B.-S., Magdalena, B., Alexandru, G., Fanny, A., Stefan, H., Georg, H., Larysa, I., Lars, K., Juha, K., Thomas, K., Mikko, L., Michael, M., Flavio, P., Robert, R., Eero, R., Amélie, S., Markku, S., Steffen, T., Rasmus, T., Peter, W., Mai, W., and Z., H.: Satellite Observations for Detecting and Forecasting Sea-Ice Conditions: A Summary of Advances Made in the SPICES Project by the EU's Horizon 2020 Programme, Remote Sensing, 12, 1214 (20p.), https://doi.org/https://doi.org/10.3390/rs12071214, 2020.

Marchenko, A., Morozov, E., Ivanov, A., Elizarova, T., and Frey, D.: Ice thickening caused by freezing of tidal jet, Russian Journal of Earth Sciences, 21, 1–8, https://doi.org/10.2205/2021ES000761, 2021.

Marsan, D., Weiss, J., Larose, E., and Métaxian, J.-P.: Sea-ice thickness measurement based on the dispersion of ice swell, The Journal of the Acoustical Society of America, 131, 80–91, https://doi.org/10.1121/1.3662051, 2012.

Marsan, D., Weiss, J., Moreau, L., Gimbert, F., Doble, M., Larose, E., and Grangeon, J.: Characterizing horizontally-polarized shear and infragravity vibrational modes in the Arctic sea ice cover using correlation methods, The Journal of the Acoustical Society of America, 145, https://doi.org/10.1121/1.5094343, 2019.

Matsumoto, M., Yoshimura, M., Naoki, K., Cho, K., and Wakabayashi, H.: GROUND PENETRATING RADAR DATA INTERPRETATION USING ELECTROMAGNETIC FIELD ANALYSIS FOR SEA ICE THICKNESS MEASUREMENT, ISPRS - International Archives of the Photogrammetry, Remote Sensing and Spatial Information Sciences, XLII-3/W7, 47–50, https://doi.org/10.5194/isprs-archives-XLII-3-W7-47-2019, 2019.

Miller, B. E. and Schmidt, H.: Observation and inversion of seismo-acoustic waves in a complex arctic ice environment, The Journal of the Acoustical Society of America, 89, 1668–1685, https://doi.org/10.1121/1.401000, 1991.

Moreau, L. and RESIF: Svalbard - Vallunden (Icewaveguide) (RESIF - SISMOB - Nodes) (dataset), https://doi.org/10.15778/RESIF.XG2019, 2019.

Moreau, L., Lachaud, C., Théry, R., Predoi, M., Marsan, D., Larose, E., Weiss, J., and Montagnat, M.: Monitoring ice thickness and elastic properties from the measurement of leaky guided waves: A laboratory experiment, The Journal of the Acoustical Society of America, 142, https://doi.org/10.1121/1.5009933, 2017.

Moreau, L., Boué, P., Serripierri, A., Weiss, J., Hollis, D., Pondaven, I., Vial, B., Garambois, S., Larose, É., Helmstetter, A., Stehly, L., Hillers, G., and Gilbert, O.: Sea Ice Thickness and Elastic Properties From the Analysis of Multimodal Guided Wave Propagation Measured With a Passive Seismic Array, Journal of Geophysical Research: Oceans, 125, e2019JC015 709, https://doi.org/10.1029/2019JC015709, 2020a.

Moreau, L., Weiss, J., and Marsan, D.: Accurate Estimations of Sea-Ice Thickness and Elastic Properties From Seismic Noise Recorded With a Minimal Number of Geophones: From Thin Landfast Ice to Thick Pack Ice, Journal of Geophysical Research: Oceans, 125, e2020JC016 492, https://doi.org/10.1029/2020JC016492, 2020b.

Moreau, L., Seydoux, L., Weiss, J., and Campillo, M.: Analysis of microseismicity in sea ice with deep learning and Bayesian inference: application to high-resolution thickness monitoring, The Cryosphere, 17, 1327–1341, https://doi.org/10.5194/tc-17-1327-2023, 2023.

Nolet, G.: A Breviary of Seismic Tomography, Cambridge University Press, Cambridge, UK, 2008.

Oliver, J., Crary, A. P., and Cotell, R.: Elastic waves in Arctic pack ice, Eos, Transactions American Geophysical Union, 35, 282–292, https://doi.org/https://doi.org/10.1029/TR035i002p00282, 1954.

https://doi.org/10.5194/egusphere-2026-2519
Preprint. Discussion started: 11 June 2026

Osborne, M. F. M. and Hart, S. D.: Transmission, Reflection, and Guiding of an Exponential Pulse by a Steel Plate in Water. I. Theory, The Journal of the Acoustical Society of America, 17, 1–18, https://doi.org/10.1121/1.1916293, 1945.

Post, E., Bhatt, U., Bitz, C., Brodie, J., Fulton, T., Hebblewhite, M., Kerby, J., Stirling, I., and Walker, D.: Ecological Consequences of Sea-Ice Decline, Science (New York, N.Y.), 341, 519–24, https://doi.org/10.1126/science.1235225, 2013.

Press, F.: Propagation of elastic waves in a floating ice sheet, Eos, Transactions American Geophysical Union, 32, 673–678, https://doi.org/https://doi.org/10.1029/TR032i005p00673, 1951a.

Press, F.: Propagation of elastic waves in a floating ice sheet, Eos, Transactions American Geophysical Union, 32, 673–678, https://doi.org/https://doi.org/10.1029/TR032i005p00673, 1951b.

Press, F. and Ewing, M.: Theory of Air-Coupled Flexural Waves, Journal of Applied Physics, 22, 892–899, https://doi.org/https://doi.org/10.1063/1.1700069, 1951.

Rajan, S. D., Frisk, G. V., Doutt, J. A., and Sellers, C. J.: Determination of compressional wave and shear wave speed profiles in sea ice by crosshole tomography—Theory and experiment, J. Acoust. Soc. Am., 93, 721–738, https://doi.org/10.1121/1.405436, 1993.

Ricker, R., Lavergne, T., Hendricks, S., Paul, S., Down, E., Killie, M. A., and Bocquet, M.: Drift-aware sea ice thickness maps from satellite remote sensing, EGUsphere, 2025, 1–27, https://doi.org/10.5194/egusphere-2025-359, 2025.

Romeyn, R. and Hanssen, A.: Microphone recording of flexural waves for estimation of lake ice thickness, Cold Regions Science and Technology, 211, 2023.

Romeyn, R., Hanssen, A., Ruud, B. O., and Johansen, T. A.: Sea ice thickness from air-coupled flexural waves, The Cryosphere, 15, 2939–2955, https://doi.org/10.5194/tc-15-2939-2021, 2021.

Sabra, K. G., Gerstoft, P., Roux, P., Kuperman, W. A., and Fehler, M. C.: Extracting time-domain Green's function estimates from ambient seismic noise, Geophysical Research Letters, 32, 2004GL021 862, https://doi.org/10.1029/2004GL021862, 2005.

Schweiger, A. J., Wood, K. R., and Zhang, J.: Arctic Sea Ice Volume Variability over 1901-2010: A Model-Based Reconstruction, Journal of Climate, 32, 4731–4752, https://doi.org/10.1175/jcli-d-19-0008.1, 2019.

Sen, M. K. and Stoffa, P. L.: Global Optimization Methods in Geophysical Inversion (second edition), Elsevier Science Publishing Co., 2013.

Serripierri, A., Moreau, L., Boue, P., Weiss, J., and Roux, P.: Recovering and monitoring the thickness, density, and elastic properties of sea ice from seismic noise recorded in Svalbard, The Cryosphere, 16, 2527–2543, https://doi.org/10.5194/tc-16-2527-2022, 2022.

Shapiro, N. M. and Campillo, M.: Emergence of broadband Rayleigh waves from correlations of the ambient seismic noise, Geophysical Research Letters, 31, 2004GL019 491, https://doi.org/10.1029/2004GL019491, 2004.

Squire, V. A., Hosking, R. J., Kerr, A. D., and Langhorne, P. J.: Moving Loads on Ice Platess, in: Moving Loads on Ice Platess, p. 236, Kluwer Academic Publishers, Dordrecht, first edition edn., https://doi.org/https://doi.org/10.1007/978-94-009-1649-4, 1996.

Stein, P. J.: Acoustic monopole in a floating ice plate, PhD dissertation, Mass. Inst. of Technol., Cambridge, 1986.

Stein, P. J., Euerle, S. E., and Parinella, J. C.: Inversion of pack ice elastic wave data to obtain ice physical properties, Journal of Geophysical Research: Oceans, 103, 21 783–21 793, https://doi.org/10.1029/98JC01269, 1998.

Stroeve, J. and Notz, D.: Changing state of Arctic sea ice across all seasons, Environmental Research Letters, 13, 103 001, https://doi.org/10.1088/1748-9326/aade56, 2018.

Trinh, P. T., Brossier, R., Métivier, L., Tavard, L., and Virieux, J.: Efficient 3D time-domain elastic and viscoelastic Full Waveform Inversion using a spectral-element method on flexible Cartesian-based mesh, Geophysics, 84, R75–R97, https://doi.org/https://doi.org/10.1190/geo2018-0059.1, 2019.

https://doi.org/10.5194/egusphere-2026-2519
Preprint. Discussion started: 11 June 2026

Tromp, J., Komattisch, D., and Liu, Q.: Spectral-Element and Adjoint Methods in Seismology, Communications in Computational Physics, 3, 2008.

Wang, Q.: Wavelet–based inversion of seismic waves in Arctic ice, PhD dissertation, Mass. Inst. of Technol., Cambridge, 1995.

Weickert, J.: Anisotropic diffusion in image processing, Treubner Verlag, Stuttgart, 1998.

Xie, Y. and Farmer, D. M.: Seismic-acoustic sensing of sea ice wave mechanical properties, J. Geophys. Res. Oceans, 99, 7771–7786, https://doi.org/https://doi.org/10.1029/93JC03483, 1994.

Xu, H., Xing, J., Zuo, G., and Wei, J.: Cross-hole acoustic tomography of Arctic sea ice: insights into temperature-driven velocity and attenuation variations, Intelligent Marine Technology and Systems, 3, https://doi.org/10.1007/s44295-025-00078-z, open Access, 2025.

Yang, T. and Yates, T.: Flexural waves in a floating ice sheet: Modeling and comparison with data, Journal of The Acoustical Society of America - J ACOUST SOC AMER, 97, 971–977, https://doi.org/10.1121/1.412076, 1995.

Yang, T. C. and Giellis, G. R.: Experimental characterization of elastic waves in a floating ice sheet, The Journal of the Acoustical Society of America, 96, 2993–3009, https://doi.org/10.1121/1.411261, 1994.